

**Thermodynamics up to the melting point in a TaVCrW high entropy alloy  
Systematic ab initio study aided by machine learning potentials**

Zhou, Ying; Srinivasan, Prashanth; Körmann, Fritz; Grabowski, Blazej; Smith, Roger; Goddard, Pooja; Duff, Andrew Ian

**DOI**

[10.1103/PhysRevB.105.214302](https://doi.org/10.1103/PhysRevB.105.214302)

**Publication date**

2022

**Document Version**

Final published version

**Published in**

Physical Review B

**Citation (APA)**

Zhou, Y., Srinivasan, P., Körmann, F., Grabowski, B., Smith, R., Goddard, P., & Duff, A. I. (2022). Thermodynamics up to the melting point in a TaVCrW high entropy alloy: Systematic ab initio study aided by machine learning potentials. *Physical Review B*, 105(21), Article 214302. <https://doi.org/10.1103/PhysRevB.105.214302>

**Important note**

To cite this publication, please use the final published version (if applicable).  
Please check the document version above.








**Copyright**

Other than for strictly personal use, it is not permitted to download, forward or distribute the text or part of it, without the consent of the author(s) and/or copyright holder(s), unless the work is under an open content license such as Creative Commons.

**Takedown policy**

Please contact us and provide details if you believe this document breaches copyrights.  
We will remove access to the work immediately and investigate your claim.

# Thermodynamics up to the melting point in a TaVCrW high entropy alloy: Systematic *ab initio* study aided by machine learning potentials

Ying Zhou <sup>1,\*</sup> Prashanth Srinivasan <sup>2</sup> Fritz Körmann <sup>3,4</sup> Blazej Grabowski <sup>2</sup> Roger Smith <sup>1</sup> Pooja Goddard <sup>1</sup> and Andrew Ian Duff <sup>5</sup>

<sup>1</sup>*School of Science, Loughborough University, LE11 3TU, United Kingdom*

<sup>2</sup>*Institute of Materials Science, University of Stuttgart, Pfaffenwaldring 55, D-70569 Stuttgart, Germany*

<sup>3</sup>*Materials Science and Engineering, Delft University of Technology, 2628 CD Delft, The Netherlands*

<sup>4</sup>*Department for Computational Materials Design, Max-Planck-Institut für Eisenforschung GmbH, 40237 Düsseldorf, Germany*

<sup>5</sup>*Scientific Computing Department, STFC Daresbury Laboratory, Warrington, WA4 4AD, United Kingdom*



(Received 28 January 2022; accepted 2 May 2022; published 10 June 2022)

Multi-principal-component alloys have attracted great interest as a novel paradigm in alloy design, with often unique properties and a vast compositional space auspicious for materials discovery. High entropy alloys (HEAs) belong to this class and are being investigated for prospective nuclear applications with reported superior mechanical properties including high-temperature strength and stability compared to conventional alloys. Computational materials design has the potential to play a key role in screening such alloys, yet for high-temperature properties, challenges remain in finding an appropriate balance between accuracy and computational cost. Here we develop an approach based on density-functional theory (DFT) and thermodynamic integration aided by machine learning based interatomic potential models to address this challenge. We systematically evaluate and compare the efficiency of computing the full free energy surface and thermodynamic properties up to the melting point at different stages of the thermodynamic integration scheme. Our new approach provides a  $\times 4$  speed-up with respect to comparable free energy approaches at the level of DFT, with errors on high-temperature free energy predictions less than 1 meV/atom. Calculations are performed on an equiatomic HEA, TaVCrW—a low-activation composition and therefore of potential interest for next generation fission and fusion reactors.

DOI: [10.1103/PhysRevB.105.214302](https://doi.org/10.1103/PhysRevB.105.214302)

## I. INTRODUCTION

The development of alloys based on multiple principal components (elements) is an area of broad interest within the material science community. These alloys—known variously as multi principal component alloys (MPCAs), high entropy alloys (HEAs) and compositionally complex alloys (CCAs)—access the interior regions of hyper-dimensional compositional space, away from the corners that are sampled by conventional alloys, opening up a vast, largely untapped expanse of compositions. HEAs can be considered a subcategory of MPCAs alongside CCAs. In this paper, we adopt the definition of HEAs as MPCAs consisting of a single extended solid solution.<sup>1</sup> Due to their multi-principal-component makeup, HEAs (and MPCAs more generally) exhibit often unique and interesting properties compared with traditional alloys including, depending on the composition, superior high-temperature strength and stability

and good corrosion resistance [1,2]. HEAs are therefore one class of materials that are under consideration as potential structural materials for next generation fission and fusion reactors, being designed to operate at higher temperatures than current reactors—in some cases up to 1000 °C. Structural materials used in current generation reactors are unsuitable for such applications [3] and new materials are required that can withstand high thermal stress at higher temperatures, more corrosive environments and higher neutron fluxes [4,5].

Another important consideration in next generation reactor design is that elements should be low activation, i.e., suitable for recycling or disposal in nonactive landfills approximately 100 years after removal from the reactor [6–8]. This precludes the use of Ni or Zr [9,10] and limits the elements from which HEA compositions can be drawn to low activation candidates Ti, V, Cr, Mn, Fe, Ta, and W. Previous studies indicated that in fusion reactors, W-based HEAs ( $W_{0.38}Ta_{0.36}Cr_{0.15}V_{0.11}$ ) showed outstanding radiation resistance [11]. The quinary system Cr-Ta-Ti-V-W and its subsystems have also been investigated in terms of phase stability and order-disorder transition temperatures [12]. In total, there are 29 different combinations of low activation elements to investigate for quinary HEAs and a vast composition space to probe for nonequiatomic compositions. Thus a methodology that can predict the properties of the materials in advance would be extremely useful.

\*y.zhou4@lboro.ac.uk

<sup>1</sup>There is not yet an agreed definition of HEAs in the literature. Aside from the definition, we adopt, some define HEAs as alloys consisting of 5 or more principal components in equiatomic or nearly equiatomic concentrations (original definition), while others use the term rather as we use MPCA in this paper to encompass both single-phase solid solutions and CCAs.

High-temperature thermodynamic properties of solids, including the thermal expansion, heat capacity, etc., are computationally expensive to calculate accurately. Using density-functional theory (DFT) and *ab initio* molecular dynamics (AIMD), the thermodynamic properties can be derived from the volume and temperature dependencies of the free energy. However, calculated directly from AIMD, this would require in the order of  $10^7$  AIMD steps [13] to achieve statistical convergence, making it infeasible.

Several approximation schemes exist in the literature which take into account phonon excitations at different levels. The most popular technique is the quasiharmonic approximation (QHA) method [14,15]. However, this approach does not take into account the anharmonicity of phonons, which can significantly affect thermodynamic properties at higher temperatures [16]. Other approaches based on effective harmonic Hamiltonians capture some of the high-temperature phonon-phonon interactions and can approximately account for temperature-induced changes [17–22].

Although computationally more challenging, numerically exact vibrational free energies can be obtained using thermodynamic integration (TI). Specifically, fully anharmonic free energies can be computed using QHA as an initial reference and AIMD runs using the Langevin thermostat. An important step in improving the efficiency of TI-based methods was the upsampled thermodynamic integration using Langevin dynamics (UP-TILD) approach [13] in which low DFT parameters (energy cutoff,  $k$ -points, etc.) were used to accelerate evaluation of TI integrals, with a post-processing “upsampling” step to bring results back to DFT accuracy.

Further improvements in efficiency were achieved with the two-stage upsampled thermodynamic integration using Langevin dynamics (TU-TILD) [23] approach, based on UP-TILD, but with the introduction of tailored interatomic potentials to characterise an intermediate reference state within the TI scheme. The purpose of these potentials is to accelerate the algorithm, with no loss of accuracy in the anharmonic free energies (converged to within  $\pm 1$  meV/atom). The TU-TILD method has already been used to calculate the free energies and *ab initio* thermodynamic properties of ZrC and vacancies in ZrC [23,24]. In these calculations, reference-free modified embedded atom method (RF-MEAM) potentials were used to characterise the intermediate reference state [25] and a  $\times 50$  improvement in efficiency was achieved in comparison with the UP-TILD approach. Thermodynamic properties to the melting point for other systems such as Cu, Ni, Al, and W have also been calculated using TU-TILD in previous works. The results show remarkable agreement to experimental data [26,27].

Our objective here is to further improve the efficiency of the TU-TILD approach to ready it for high throughput screening of MPCAs. To achieve this we use machine learned interatomic potentials, specifically moment tensor potentials (MTPs), to define our intermediate reference state. The efficiency of MTPs in predicting DFT energies, forces and phase space for a disordered five-component HEA has been demonstrated earlier for the NbMoTaVW system [28] for a single  $(V, T)$  point. The DFT free energy and atomic forces at 3000 K were compared to that predicted by the MTP, an embedded-atom method (EAM) potential [29,30], an effective

harmonic potential, and a 0 K harmonic potential. Of these, the MTP-predicted forces had by far the lowest errors and the corresponding MTP free energy was more accurate by an order of magnitude, thereby making the MTPs the best candidate for the intermediate state in the TU-TILD scheme. In the present work, we extend this approach to calculate free energies for an entire grid of  $(V, T)$  points from which thermodynamic properties such as the lattice expansion, bulk modulus and specific heat are calculated.

Throughout our calculations we perform a critical analysis of various parts of the TU-TILD scheme in terms of the accuracy of the predicted properties and the efficiency of the overall approach. Efficiency gains are achieved by reducing the number of separately optimised potentials required to define the intermediate reference and by exploring the efficacy of different initial references. Moreover, since MTPs are extremely effective in replicating the DFT phase space, we also propose a modification to the TU-TILD method whereby the most expensive second TI stage is completely avoided, with only a nominal change in the accuracy of the results.

We apply our accelerated scheme to the low-activation equiatomic body-centred cubic (BCC) TaVCrW system as a first application of TU-TILD in computing the full free energy surface and thermodynamic properties of an MPCA.

## II. METHODOLOGY AND COMPUTATIONAL DETAILS

The Helmholtz energy of a system, referred hereafter as the total free energy, can be expressed as the sum of different contributions. For a nonmagnetic, fixed chemical configuration (i.e., a chemically ordered or a particular disordered atomic arrangement), the total free energy can be adiabatically decomposed as

$$F(V, T) = E_{0K}(V) + F^{\text{el}}(V, T) + F^{\text{vib}}(V, T) + F^{\text{cpl}}(V, T), \quad (1)$$

where  $E_{0K}$  is the total energy at  $T = 0$  K,  $F^{\text{el}}$  is the electronic free energy of the static lattice,  $F^{\text{vib}}$  is the free energy coming from atomic vibrations and  $F^{\text{cpl}}$  represents adiabatic coupling terms, i.e., the effect of vibrations on the electronic free energy and vice-versa [26]. The first two terms in Equation (1) are computed using inexpensive DFT calculations. The more challenging vibrational free energy and the coupling contribution are calculated using the TU-TILD scheme. In a recent work [12], Monte-Carlo simulations predicted an order-disorder temperature of around 1300 K for TaVCrW below which there was short-range-ordering. Configurational entropy will thus have an effect on the thermodynamic property predictions around this temperature, but this is beyond the scope of the present work.

Here, we focus primarily on high-temperature thermodynamic properties and for all calculations, we assume a fully disordered BCC solid solution across the entire temperature range. The chemical disorder is modelled by a 128-atom BCC TaVCrW special quasirandom structure (SQS) [31]. The structure is created in such a way that the correlation function of the first two shells of the neighbor-pair interactions is minimized. The accuracy of the total vibrational free energy was tested between three different SQS for selected  $(V, T)$  points for which it varied by less than 1 meV/atom. Hence

the final thermodynamic properties are presented here for a single SQS.

Once  $F(V, T)$  is known over the relevant volume-, temperature-range, a free energy surface can be parameterised. A Legendre transformation on the free energy surface gives the Gibbs energy  $G(P, T) = F(V, T) + PV$ . From this, thermodynamic properties including the temperature-dependent lattice constant  $a_{\text{lat}}(T)$ , isothermal bulk modulus  $B_T(T)$  and isobaric heat capacity  $C_P(T)$  can be computed [32,33] as given by

$$a_{\text{lat}}(T) = \sqrt[3]{2V(T)} \quad \text{with} \quad V(T) = \left( \frac{\partial G(P, T)}{\partial P} \right)_T, \quad (2)$$

$$B_T(T) = \frac{1}{\kappa} \quad \text{with} \quad \kappa = -\frac{1}{V} \left( \frac{\partial^2 G(P, T)}{\partial P^2} \right)_T, \quad (3)$$

and

$$C_P(T) = -T \left( \frac{\partial^2 G(P, T)}{\partial T^2} \right)_P. \quad (4)$$

The DFT energies and forces entering the different free energy contributions were calculated with the VASP software package using the projector augmented wave (PAW) method [34–37]. Both GGA and LDA exchange-correlation functionals were used [38,39]. Semi-core  $p$  electrons were included as valence states.

### A. Energy of the static lattice

The first term in Eq. (1),  $E_{0\text{K}}(V)$  was obtained by fitting the Vinet equation of state [40] to  $E_{0\text{K}}$  values calculated across a relevant set of volumes. The temperature-dependent part of the static electronic free energy  $F^{\text{el}}(V, T)$  was computed as [33]

$$F^{\text{el}}(V, T) = F_{\text{tot}}^{\text{el}}(V, T) - E_{0\text{K}}(V), \quad (5)$$

where  $F_{\text{tot}}^{\text{el}}$  is the total electronic free energy according to the finite temperature formulation of DFT [41] calculated at a finite electronic temperature with the corresponding Fermi smearing. In our calculations, electronic free energies were extracted from DFT runs on a mesh of 10 temperatures and 9 volumes and the pure  $T$  dependent contribution was obtained by subtracting the energy at  $T = 0$  K. These DFT runs were performed with a plane wave cutoff of 650 eV and a  $k$ -point grid of  $5 \times 5 \times 5$ . A dense temperature sampling was obtained using a physically motivated fit  $F^{\text{el}}(T) = -\frac{1}{2}TS^{\text{el}}(T)$ , with

$$S^{\text{el}}(T) = -2k_B \int d\epsilon N^{\text{el}}(T) [f \ln f + (1-f) \ln(1-f)], \quad (6)$$

where  $f = f(\epsilon, T)$  is the Fermi-Dirac distribution function and  $N^{\text{el}}(T)$  represents an energy-independent electronic density of states [33].  $N^{\text{el}}(T)$  was used as a fitting quantity by expanding it to a fourth-order polynomial in  $T$ . Following this, the volume dependence was parametrized with a fourth-order polynomial in  $V$ . One needs to keep in mind that this term only calculates the electronic free energy of the static lattice. At higher temperatures, the atoms are no longer in their ideal positions, and hence the electronic free energy is affected by

high-temperature vibrations. This change in the electronic free energy is represented by the  $F^{\text{cpl}}(V, T)$  term in Eq. (1).

### B. Vibrational free energy including coupling

The total vibrational free energy including explicit anharmonic contributions was calculated at DFT accuracy using the TU-TILD scheme. TU-TILD provides the vibrational free energy difference between an initial reference state that describes the system and DFT, which also accounts for the change in the electronic free energy due to vibrations  $F^{\text{cpl}}(V, T)$ . This can be written as

$$F^{\text{vib}}(V, T) + F^{\text{cpl}}(V, T) = F^{\text{ref}}(V, T) + \Delta F^{\text{ref} \rightarrow \text{DFT}}(V, T), \quad (7)$$

where  $F^{\text{ref}}(V, T)$  is the free energy calculated using the initial reference and  $\Delta F^{\text{ref} \rightarrow \text{DFT}}(V, T)$  is the remaining contribution calculated using TU-TILD.

#### 1. Reference state for the vibrational free energy

Earlier TU-TILD-based studies used the QHA as a reference [23,26,28]. Using the finite displacement method [39,42,43] this requires DFT calculations for all symmetry-inequivalent atomic displacements to obtain the harmonic force constants matrix for a given volume. For a 128-atom disordered SQS, this would require 384 DFT calculations which would be prohibitively expensive. Instead we opt here for more computationally efficient initial reference models, while carefully testing to ensure that the choice of the initial reference does not affect the total free energy.

The first reference state considered was an Einstein solid [44], in which all atoms are assumed to be oscillating with the same single frequency. We assessed three different Einstein solids as an initial reference: (i) with a fixed force constant of 5.83 eV/Å<sup>2</sup> (average frequency of 4.03 THz), (ii) with a fixed force constant of 12.63 eV/Å<sup>2</sup> (average frequency of 5.93 THz), and (iii) with volume-dependent force constants ranging from 5.83 to 12.63 eV/Å<sup>2</sup>. We refer to these models hereafter as Einstein(1), Einstein(2), and qh-Einstein, respectively. The frequencies for Einstein(1) and Einstein(2) were chosen as follows. Firstly, we computed the 0 K QH phonon frequencies of the four unaries at the volume corresponding to room temperature. The mean value of these frequencies was found to be 9.23 eV/Å<sup>2</sup>. To this we subtracted and added approximately one-third of the value to make a lower and upper bound that subsequently corresponds to Einstein(1) and Einstein(2), respectively. Choosing different Einstein solids as reference states was done primarily to evaluate the accuracy of the methodology. We will show later (in Table III) that these reference frequencies do not affect the total free energies.

The second reference model considered was an effective QH model where the force constants were fit to high-temperature AIMD data, similar in nature to the temperature-dependent effective harmonic potentials [19,45]. Four effective harmonic force constants were fit to atomic forces from AIMD runs at four different volumes (corresponding to lattice constants 3.035, 3.095, 3.175, and 3.255 Å) at 500 K using the implementation in the S/PHI/nX code [46]. Each effective force constant was then parameterised by a third-order polynomial in volume which served

as the reference for each volume point in the TI. From the volume-dependent effective force constants, effective phonon frequencies were calculated by constructing the dynamical matrix and solving the eigenproblem [47,48]. We refer to this reference as “qh-effective” in this work.

For each of the above cases, the reference free energy  $F^{\text{ref}}(V, T)$  (per atom) was analytically calculated from the corresponding frequencies as given by

$$F^{\text{ref}} = \frac{1}{N} \sum_{i=1}^{3N} \left\{ \frac{1}{2} \hbar \omega_i^{\text{ref}} + k_B T \ln \left[ 1 - \exp \left( -\frac{\hbar \omega_i^{\text{ref}}}{k_B T} \right) \right] \right\}, \quad (8)$$

where  $N$  is the number of atoms and the summation is over the  $3N$  frequencies  $\omega_i^{\text{ref}}$ . In the Einstein models, the frequencies corresponding to the same species were the same. For the “qh-effective” reference, the free energies were recalculated on a much denser  $20 \times 20 \times 20$   $q$ -point grid in reciprocal space. For a temperature mesh with 1 K steps, the reference free energy was then parameterised using 11 volumes with a third order polynomial in  $V$ .

## 2. TU-TILD

In order to account fully for anharmonicity, we performed TU-TILD calculations from each of the references up to DFT. According to the conventional TU-TILD formalism that has been well established for known systems in the literature [23,26–28], the free energy difference between the reference and full DFT energy is given by

$$\begin{aligned} \Delta F^{\text{ref} \rightarrow \text{DFT}} &= \Delta F^{\text{ref} \rightarrow \text{MTP}} + \Delta F^{\text{MTP} \rightarrow \text{DFT}} + \langle \Delta E \rangle^{\text{up}} \\ &= \int_0^1 d\lambda_1 \langle E^{\text{MTP}} - E^{\text{ref}} \rangle_{\lambda_1} \\ &\quad + \int_0^1 d\lambda_2 \langle E_{\text{low}}^{\text{DFT}} - E^{\text{MTP}} \rangle_{\lambda_2} + \langle \Delta E \rangle^{\text{up}}, \end{aligned} \quad (9)$$

with

$$\langle \Delta E \rangle^{\text{up}} = -k_B T \ln \left\langle \exp \left( -\frac{E_{\text{high}}^{\text{DFT}} - E_{\text{low}}^{\text{DFT}}}{k_B T} \right) \right\rangle_{\text{low}}. \quad (10)$$

In Eq. (9), the  $\lambda$ 's are coupling parameters between the initial ( $\lambda = 0$ ) and final ( $\lambda = 1$ ) states in a TI for which the energy of the coupled system is  $E_\lambda = (1 - \lambda)E^{\text{initial}} + \lambda E^{\text{final}}$  and for which the corresponding atomic forces are  $\mathbf{F}_\lambda^{(i)} = (1 - \lambda)\mathbf{F}^{(i),\text{initial}} + \lambda\mathbf{F}^{(i),\text{final}}$  (with  $i$  labeling the atoms), driving the Langevin dynamics.  $\langle \dots \rangle$  denotes ensemble averaging, “ref” corresponds to the reference model [Einstein(1), Einstein(2), qh-Einstein or qh-effective in this case], “MTP” is an intermediate interatomic potential (described in Sec. II B 3) that is fit to DFT energies and forces (the intermediate potential can be any interatomic model, in this work we use MTPs),  $\Delta F^{\text{ref} \rightarrow \text{MTP}}$  is the free energy difference between the reference and potential,  $\Delta F^{\text{MTP} \rightarrow \text{DFT}}$  is the free energy difference between the potential and low-parameter DFT and  $\langle \Delta E \rangle^{\text{up}}$  is the upsampled energy calculated using the free energy perturbation theory [49] from configurations from a low-parameter AIMD run.  $E_{\text{low}}^{\text{DFT}}$  and  $E_{\text{high}}^{\text{DFT}}$  are DFT energies with low and high convergence parameters, respectively.

The  $\Delta F^{\text{ref} \rightarrow \text{DFT}}$  calculations were performed on a dense mesh of 10 temperatures from 250 to 2500 K and 11 volumes

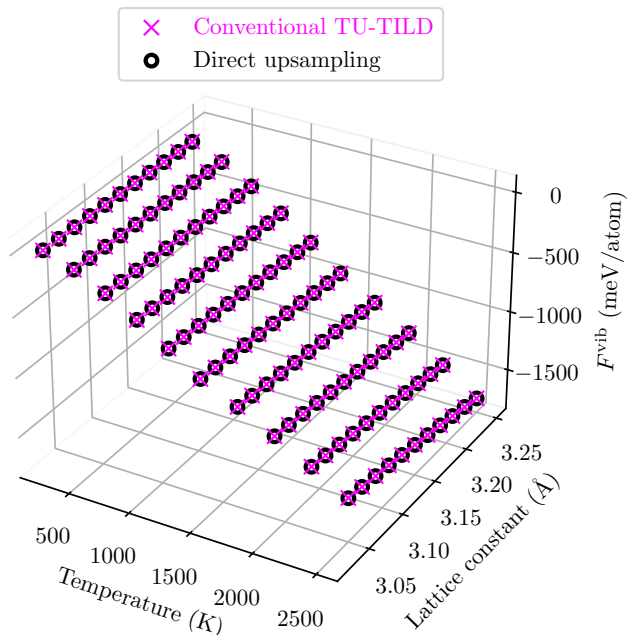


FIG. 1. Grid of  $(V, T)$  points on which TU-TILD and direct upsampling calculations were performed. Vibrational free energies calculated using both methodologies using the GGA exchange-correlation functional are plotted at each point for comparison (magenta dots for TU-TILD and black dots for direct upsampling). The deviation in the magenta and black dots are within  $\pm 1.5$  meV/atom.

for each temperature (cf. Fig. 1). Both the AIMD run and the fitted interatomic potentials predict a solid phase up to 2500 K. Hence we chose 2500 K, which is also the highest temperature to which an interatomic potential was fitted to, as the temperature upper bound for the free energy calculations. One should keep in mind that this is not the actual melting temperature, but a value close to it, and one for which the alloy is most certainly in a solid phase. In order to precisely calculate the melting temperature, more advanced techniques [50] are needed. As discussed earlier, different sets of calculations were performed to assess the four different initial references (two volume-independent Einstein solids, qh-Einstein, and qh-effective). The integrals in Equation (9) were numerically calculated using a tangential fit through the data points.  $E^{\text{ref}}$  was analytically calculated,  $E^{\text{MTP}}$  using LAMMPS [51,52] and  $E_{\text{low}}^{\text{DFT}}$  and  $E_{\text{high}}^{\text{DFT}}$  using VASP.

Thermodynamic integration was performed on a  $11 \times 10$   $(V, T)$  mesh as mentioned above. The first TI from “ref” to MTP to compute  $\Delta F^{\text{ref} \rightarrow \text{MTP}}$ , which is computationally extremely cheap, was done for a set of 20  $\lambda$  points for each  $(V, T)$ . Each Langevin dynamics run was performed for 300 000 steps with a time step of 0.5 fs. The second TI from MTP to “DFT-low” to compute  $\Delta F^{\text{MTP} \rightarrow \text{DFT}}$ , which is significantly more expensive since it involves DFT calculations, was done for a set of 5  $\lambda$  points for each  $(V, T)$ . Following a pre-equilibration using the interatomic potential for 1000 steps, each Langevin dynamics run was performed for 500 steps with a time step of 2 fs. During this stage, low convergence DFT parameters were used—an energy cutoff of 300 eV and a  $2 \times 2 \times 2$   $k$ -point grid. The DFT energies were

calculated with the electronic temperature set equal to the system temperature. In this way, the temperature-dependent electronic free energy is properly included in the  $\Delta F^{\text{MTP} \rightarrow \text{DFT}}$  values. The number of steps and  $\lambda$  values were chosen to ensure convergence of the  $\Delta F^{\text{ref} \rightarrow \text{DFT}}$  to within 1 meV/atom. In Eq. (10), the upsampled DFT energies were calculated using stricter parameters—a 450 eV energy cutoff and a  $4 \times 4 \times 4$   $k$ -point grid and again with the electronic temperature turned on, on 10 configurations from the low-parameter DFT run, until  $\langle \Delta E \rangle^{\text{up}}$  converged. Once the  $\Delta F^{\text{ref} \rightarrow \text{DFT}}$  calculations were finished for the set of  $(V, T)$ , we used the values to fit a much denser surface in  $(V, T)$ . Using the analytical formula derived in Ref. [13], a smooth anharmonic free energy surface was fitted using a renormalized frequency with basis functions  $1, T, V, V^2$ , and  $V^3$ .

The performance of the above described TU-TILD relies on the accuracy and robustness of the intermediate interatomic potential. The more accurately the interatomic potential describes the configurational phase space and energy of the system, the fewer the number of expensive Langevin dynamics runs needed to achieve statistical convergence on the DFT energies. Here we fitted machine-learning-based MTPs and used them as the intermediate potential in the TU-TILD scheme.

### 3. MTP fitting

MTPs are a class of machine learned potentials based on atomic environment descriptors and linear regression [53]. MTPs describe the local atomic environment of the  $i$ th atom by the moments of inertia of neighboring atoms, with the moments given by

$$M_{n,v} = \sum_j f_{n,i,j}(r_{ij}) \underbrace{\mathbf{r}_{ij} \otimes \mathbf{r}_{ij} \otimes \dots \otimes \mathbf{r}_{ij}}_{v \text{ times}}, \quad (11)$$

where the radial functions  $f_{n,i,j}(r_{ij})$  define shells,  $n = 0, 1, \dots$ , around the  $i$ th atom, with contributions from atom  $j$  which can depend on the types of atoms  $i$  and  $j$ . Different tensor contractions of these moments  $M$  form basis functions of the MTP. A linear combination of these basis functions is parameterised to reproduce energy, atomic forces and stress data from AIMD runs. MTPs have been shown to outperform other machine learning based potentials [54] and more conventional EAM-based potentials [28] which prompted our use of them.

The MTPs were fit using the MLIP package [53,55]. First, AIMD simulations were carried out at 500, 1500, 2000, and 2500 K and 11 volumes at each temperature for 5 ps. The volume range at each temperature was chosen based on the Debye-Grüneisen approximation [56] from the energy-volume curve in Sec. II A. A cutoff of 300 eV, a  $k$ -point mesh of  $2 \times 2 \times 2$  and the corresponding exchange correlation were used for generating the fitting database. Separate MTPs were fit to configurations corresponding to each temperature (configurations from all volumes were included for a particular temperature). The MTPs were of level 16 with 608 parameters and fitting weights for the energies, atomic forces, and stresses were set to 1,  $0.1 \text{ \AA}^2$ , and  $0.001 \text{ \AA}^6$ , respectively.

Regarding the application of our fitted MTPs in our TI, we analysed two scenarios. In the first case, we performed

TI calculations using all the four MTPs depending on the temperature of the TILD run. This is similar to previous studies of multicomponent alloys using TU-TILD (although in these studies potentials were computed and applied for different volumes rather than temperatures) [23,24]. In the second case, we explored a new approach, where we used only the MTP potential that was fit to 2500 K AIMD runs for the entire temperature-range during TU-TILD. Here, it is beneficial to use the highest temperature fitted MTP for the entire temperature range (in comparison to fitting a single MTP to configurations from different temperatures) since the volume range and the configurations spanned by the highest temperature MD runs are diverse enough to serve as a good training set for an efficient single MTP. The final thermodynamic properties and computational efficiency were compared in both cases, where either four MTPs were used or where a single MTP was used across the entire temperature-range.

### 4. Direct upsampling

Apart from systematically investigating multiple reference potentials and MTPs in the conventional TU-TILD formalism, an additional improvement to the TU-TILD methodology is proposed here which is inspired by the exceptional performance of MTPs in replicating the DFT configurational space. According to this proposition, the more expensive  $\Delta F^{\text{MTP} \rightarrow \text{DFT}}$  calculation in the TU-TILD scheme can be completely avoided.

A similar modification was suggested earlier [24] where thermodynamic properties in a ZrC system were calculated only up to the accuracy of the intermediate interatomic potential. The results compared well to DFT since there was no significant change in the electronic free energy with temperature and the intermediate interatomic potential was able to capture the phonon-phonon interactions accurately. This is, however, insufficient for the here investigated refractory system because of the significant temperature-dependent electronic free energy changes. Hence, apart from avoiding the second stage of TU-TILD, we perform here direct upsampling on configurations generated by the interatomic potential in order to directly capture the difference in free energies (including the electronic contribution) between the interatomic potential and DFT.

The upsampling is performed directly on configurations generated from MD runs using the MTP. According to this modified formalism, referred from here on as *direct upsampling*,  $\Delta F^{\text{ref} \rightarrow \text{DFT}}$  from Eq. (7) can be decomposed as

$$\begin{aligned} \Delta F^{\text{ref} \rightarrow \text{DFT}} &= \Delta F^{\text{ref} \rightarrow \text{MTP}} + \langle \Delta E \rangle^{\text{up-new}} \\ &= \int_0^1 d\lambda \langle E^{\text{MTP}} - E^{\text{ref}} \rangle_\lambda + \langle \Delta E \rangle^{\text{up-new}}, \end{aligned} \quad (12)$$

with

$$\langle \Delta E \rangle^{\text{up-new}} = -k_B T \ln \left\langle \exp \left( -\frac{E^{\text{DFT}} - E^{\text{MTP}}}{k_B T} \right) \right\rangle_{\text{MTP}}, \quad (13)$$

where  $\langle \Delta E \rangle^{\text{up-new}}$  is the upsampled energy calculated using free energy perturbation theory directly from configurations generated by the MTP. The high-parameter DFT conditions in our application of the proposed direct-upsampling method

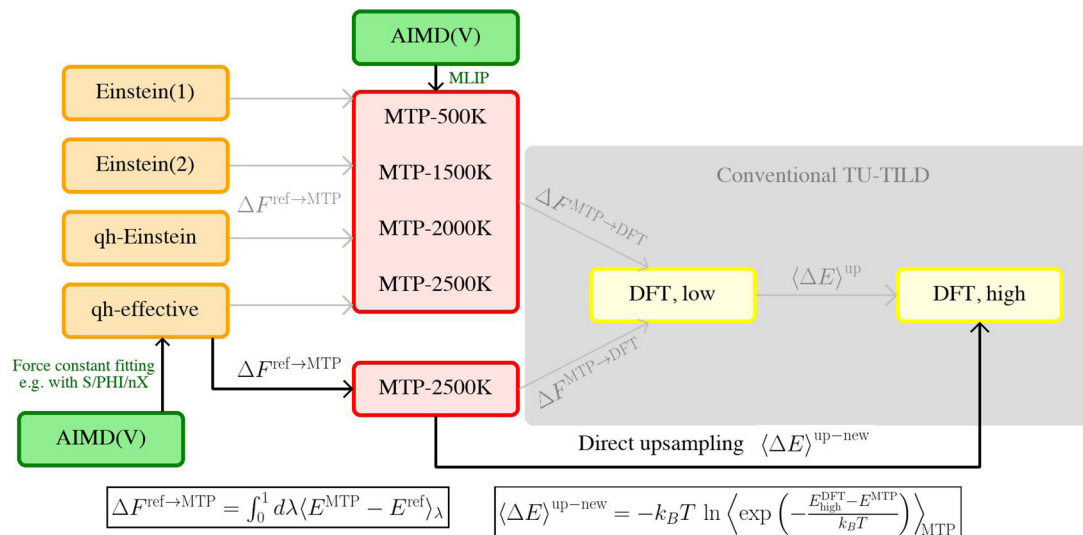


FIG. 2. Flowchart summarising the standard TU-TILD approach and the improvements developed herein. We compare four different initial reference models (orange boxes), where Einstein(1) and Einstein(2) correspond to two different Einstein solids with different fixed frequencies, qh-Einstein is a volume-dependent Einstein solid and qh-effective is a volume-dependent effective harmonic model. Two different scenarios for the intermediate MTP potential are considered (red boxes), where we compare using multiple MTPs that have been fitted to different temperatures and a single 2500 K fitted MTP, for the entire temperature range. The steps inside the grey box are a part of the standard TU-TILD. In this work, we have improved on this by directly upsampling from the MTP stage ( $\langle \Delta E \rangle^{up-new}$ ). After the current extensive study, the authors recommend the direct-upsampling method (marked with black arrows) for future studies.

were the same as described in Sec. II B 2, where the DFT energies were calculated with the electronic temperature equal to the system temperature. The temperature-dependent electronic free energy gets indirectly included in the  $\langle \Delta E \rangle^{up-new}$  term. For each  $(V, T)$ , 10 configurations were chosen by which  $\langle \Delta E \rangle^{up-new}$  was converged to within 1 meV/atom.

Similar to the conventional TU-TILD, direct upsampling was also performed on a  $11 \times 10 (V, T)$  grid. To visualize the density of the mesh on which TU-TILD and direct upsampling calculations were performed, Fig. 1 shows the calculated vibrational free energy values on the  $(V, T)$  grid points. The comparison of the free energy values using both methodologies will be discussed later in Sec. III F.

Once the upsampling calculations were finished, we applied a surface fitting to a much denser  $(V, T)$  grid with the same basis functions as in Sec. II B 2.

After  $E_{0K}(V)$ ,  $F^{el}(V, T)$  (both Sec. II A) and  $F^{vib}(V, T)$ ,  $F^{cpl}(V, T)$  (both Sec. II B) were calculated on a dense  $(V, T)$  grid, they were summed up to obtain the full free energy  $F(V, T)$  from which thermodynamic properties including lattice expansion, isobaric heat capacity and bulk modulus were numerically calculated using Eqs. (2)–(4), respectively. The entire workflow describing TU-TILD and direct upsampling for vibrational free energy calculation is shown in Fig. 2. The different reference potentials are in orange boxes and the two different intermediate MTP scenarios are in red boxes. The steps inside the grey box, which belong to the conventional formalism, can be completely avoided in our proposed modification. This new modified TILD methodology with direct upsampling—which is the most optimal procedure for thermodynamic property predictions—is represented with thick black arrows and formulas in the flowchart.

### III. RESULTS AND DISCUSSION

#### A. MTP fitting

As detailed in Sec. II B 3, we fitted different MTPs to AIMD runs performed at 500, 1500, 2000, and 2500 K. Table I shows the root mean square errors (RMSE) in energies and atomic forces for each of the MTPs with respect to the DFT values in the corresponding dataset. Each of the MTPs is fitted to within 3 meV/atom accuracy. The RMSE in atomic forces increases with increasing temperature of the AIMD runs from which configurations are taken. Since we also tested the performance of a single 2500 K MTP across the entire temperature range, the RMS errors in energies and forces predicted by MTP-2500K compared to the AIMD data at all four temperatures is shown in Table II.

The performance of MTPs as an intermediate state in the TU-TILD scheme can also be assessed by comparing the differences in energies and forces during TI to DFT. In Fig. 3, we show one such comparison. Here, the MTP that was fit to 2500 K AIMD runs was used to run Langevin dynamics at 2500 K and at a lattice constant of 3.09 Å. Figure 3(a) shows

TABLE I. RMS errors in energies and atomic forces of the fitting dataset for each of the MTPs with respect to the DFT values.

Potential	RMSE in energies (meV/atom)	RMSE in forces (eV/Å)
MTP-500K	2.02	0.11
MTP-1500K	2.78	0.18
MTP-2000K	2.47	0.21
MTP-2500K	2.36	0.25

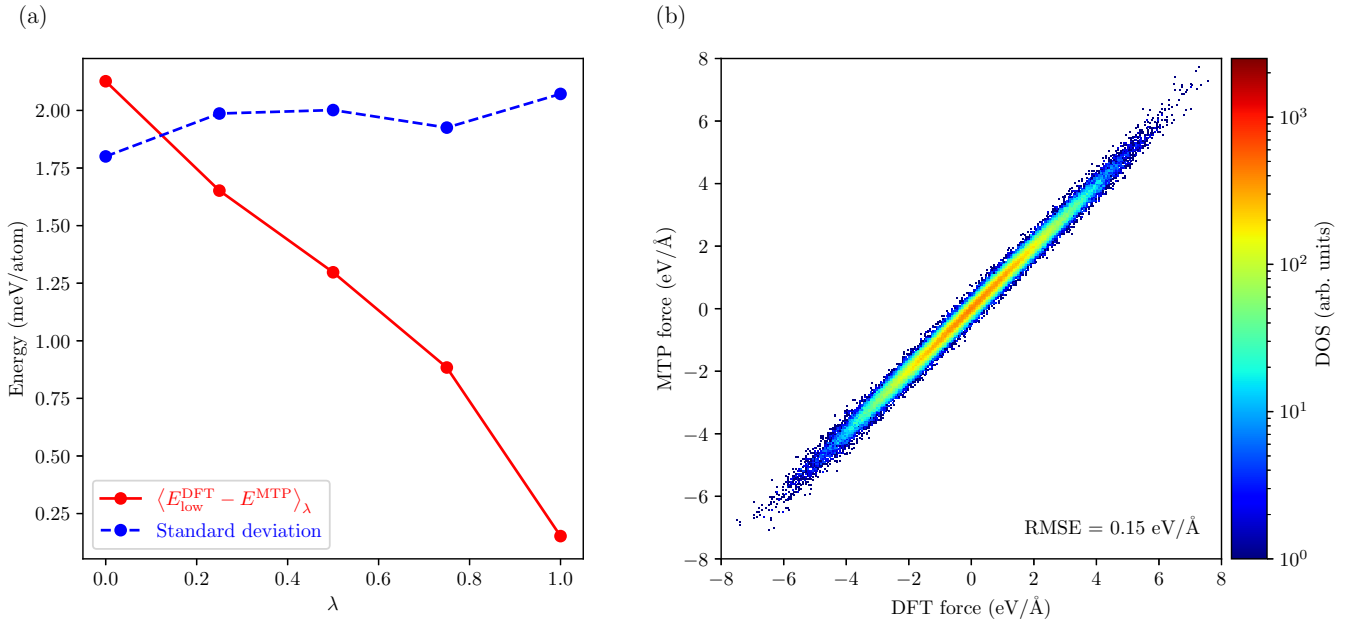


FIG. 3. (a)  $\langle E_{\text{low}}^{\text{DFT}} - E^{\text{MTP}} \rangle_{\lambda}$  and standard deviation as a function of  $\lambda$  at 2500 K and 3.09 Å during a TI from MTP to DFT-low and (b) the corresponding atomic force correlation between MTP-2500 and DFT for  $\lambda = 1$ .

the variation of  $\langle E_{\text{low}}^{\text{DFT}} - E^{\text{MTP}} \rangle_{\lambda}$  and the standard deviation of the energy difference as a function of  $\lambda$ . Figure 3(b) shows the atomic force correlation between MTP and DFT for  $\lambda = 1$ . The area under the red curve, which gives the free energy difference between the MTP and DFT, is around 1 meV/atom, and the standard deviation is close to 2 meV/atom for all  $\lambda$  values. The RMSE in the atomic forces is 0.15 eV/Å for  $\lambda = 1$ . Although not explicitly shown here, the accuracy of all the MTPs for TI calculations at other temperatures and volumes is equally good, with gradually increasing free energy difference with  $V$  and  $T$ . Table I and Fig. 3 convey the fact that MTPs are extremely effective as an intermediate state in TU-TILD.

### B. Initial reference models in TU-TILD

We investigated four different reference models in terms of their efficiency and practicability. Figure 4 shows the relevant  $\langle E^{\text{MTP}} - E^{\text{ref}} \rangle_{\lambda}$  curves as a function of  $\lambda$  between the reference models Einstein(1), Einstein(2), qh-Einstein, and qh-effective, and the 2500 K fitted MTP at 2500 K and 3.16 Å lattice constant. The curve for the qh-Einstein reference falls in between the two Einstein(1) and (2) curves, which is rea-

sonable because it corresponds to an interpolation between these two endpoints. Further, the qh-Einstein reference shows a similar behavior as the qh-effective reference, although the latter shows a smoother  $\lambda$  dependence. Upon adding the reference free energy  $F^{\text{ref}}$  to  $\Delta F^{\text{ref} \rightarrow \text{MTP}}$  (the free energy difference between the reference and the 2500 K MTP) for the four different references, we obtain the total vibrational free energy predicted by the 2500 K MTP.  $\Delta F^{\text{ref} \rightarrow \text{MTP}}$  is

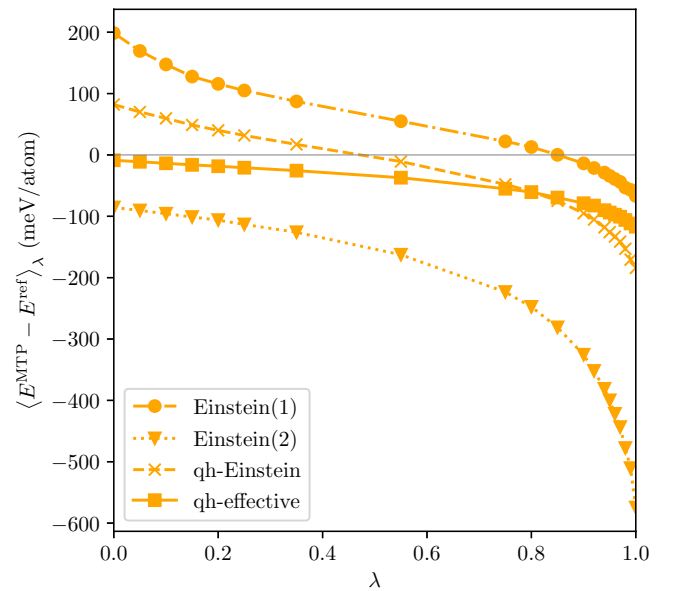


FIG. 4.  $\langle E^{\text{MTP}} - E^{\text{ref}} \rangle_{\lambda}$  versus  $\lambda$  during TI between the different references and the 2500 K MTP at 2500 K. Einstein(1) and Einstein(2) represent Einstein models with spring constants 5.83 to 12.63 eV/Å<sup>2</sup>, respectively, qh-Einstein is a volume-dependent Einstein solid reference and qh-effective denotes a volume-dependent effective harmonic reference.

TABLE II. RMS errors in energies and atomic forces predicted by MTP-2500K at all four temperatures with respect to DFT.

MTP-2500K	RMSE in energies (meV/atom)	RMSE in forces (eV/Å)
AIMD 500K	1.95	0.08
AIMD 1500K	2.46	0.10
AIMD 2000K	4.48	0.14
AIMD 2500K	2.36	0.25



TABLE III. Vibrational free energy up to the 2500 K MTP ( $F^{\text{vib}} = F^{\text{ref}} + \Delta F^{\text{ref} \rightarrow \text{MTP}}$ ) in meV/atom using the four different references at 2500 K with lattice constant 3.16 Å.

Reference	$F^{\text{ref}}$	$\Delta F^{\text{ref} \rightarrow \text{MTP}}$	$F^{\text{vib}}$
Einstein(1)	-1675.49	65.09	-1610.40
Einstein(2)	-1424.03	-185.93	-1609.96
qh-Einstein	-1597.70	-12.34	-1610.04
qh-effective	-1566.20	-43.21	-1609.41

calculated as the area under the curves. These values are tabulated and summed up to obtain the vibrational free energy in Table III. We observe that the final vibrational free energy values are within  $\pm 1$  meV/atom irrespective of the reference. This is shown here for a single  $(V, T)$  point, but it remains valid for all data points at which free energies are calculated. In each case, the difference in the free energy based on the reference model is compensated by the free energy difference during TI. In Fig. 4, the qh-effective reference gives the smoothest  $\lambda$ -dependence of all the curves. Avoiding strong nonlinear dependencies in particular at large  $\lambda$  values leads to the smallest error while calculating the area under the curve ( $\Delta F^{\text{ref} \rightarrow \text{MTP}}$ ). Therefore we use qh-effective as the reference for all future results described in this article.

### C. Thermodynamic properties using the conventional TU-TILD approach

First we demonstrate the results obtained using qh-effective as initial reference, four MTPs across the temperature range, the conventional TU-TILD formalism (i.e.,

including the second TI), and using the GGA exchange correlation functional. During TI at a given temperature, an MTP that was fit either to that particular temperature or a slightly higher temperature was used (MTP-2500K for 2500 and 2250 K, MTP-2000K for 2000 and 1750 K and so on). Once the full free energy surface  $F(V, T)$  was obtained, thermodynamic properties were numerically calculated by taking the corresponding derivatives along different directions. Figure 5 shows the lattice constant  $a_{\text{lat}}$ , the isobaric heat capacity  $C_P$  and the bulk modulus  $B_T$  as a function of temperature, computed at different levels of approximation: high-temperature effects up to the accuracy of the qh-effective model given by the orange lines, including the temperature-dependent electronic contributions on the static lattice given by green lines, including anharmonicity as predicted by the MTP given by the blue lines, including the temperature-dependent change in electronic free energy due to vibrations (coupling) given by the black lines and up to full DFT accuracy given by the magenta dots.

The 0 K lattice constant is calculated as 3.105 Å, which is very close to the calculated value from Vegard's law [57] using the DFT-GGA 0 K lattice constants of the unaries (3.088 Å) and using the experimental lattice constants of the unaries (3.098 Å). Similarly, the 0 K bulk modulus is predicted to be 223 GPa, which is in close proximity to the Vegard's law calculated value of 236 GPa using unary GGA calculations and 215 GPa from unary experimental values [58–60]. The static electronic contribution has a considerable effect on the thermodynamic properties at higher temperatures as represented by the green shaded region in Fig. 5.

Including anharmonicity (represented by the blue shaded region; at the level of the MTP and with respect to the qh-effective reference) enhances the temperature dependence of

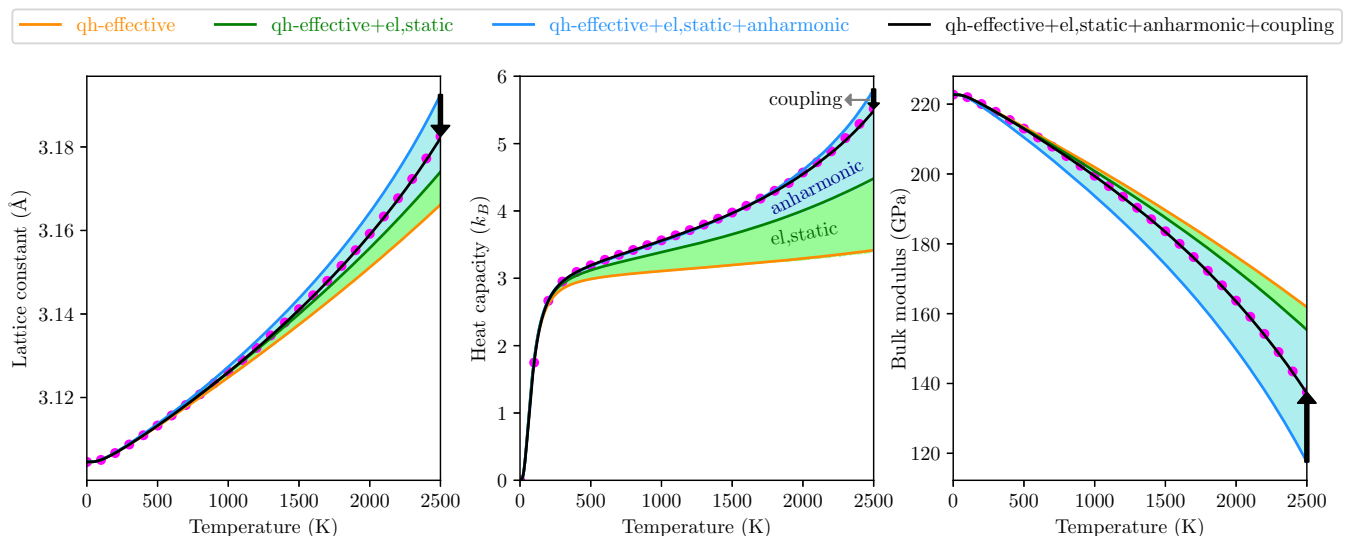


FIG. 5. Lattice constant, isobaric heat capacity and bulk modulus as a function of temperature for TaVCrW as predicted by the conventional TU-TILD approach using the GGA exchange correlation function; qh-effective was used as the reference and four MTPs were used across the temperature range in the TU-TILD calculation. The thermodynamic properties are shown to different levels of approximation. The orange, green, blue and black lines correspond to properties predicted to qh-effective, qh-effective including static electronic, MTP, and low-parameter DFT including coupling accuracy respectively. The magenta dots are up to full DFT accuracy. The green and blue shaded regions represent the contribution of the static electronic and anharmonic free energies to the thermodynamic properties respectively. The black arrows (shown only at 2500 K) denote the shift in the thermodynamic properties upon including coupling effects.

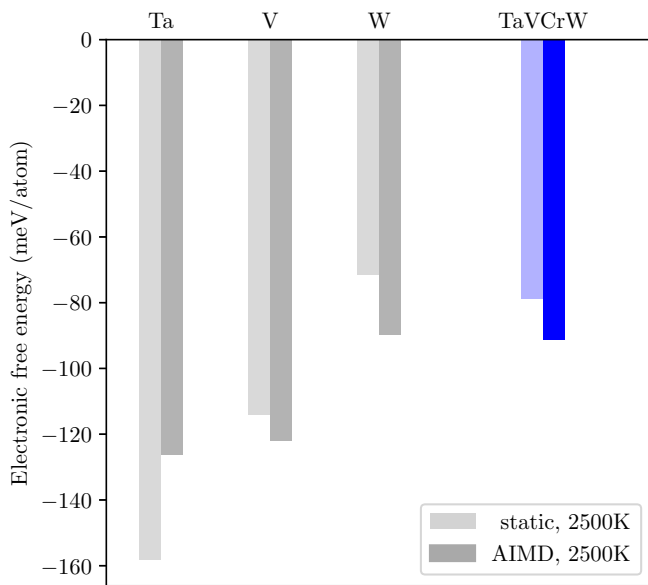


FIG. 6. Comparison of the electronic free energies extracted from AIMD runs—including the effect of vibrations—with those computed for an ideal static lattice at 2500 K. The energies are compared for the TaVCrW HEA with three unaries that it is composed of. Unary Cr is not shown here due to the challenges involved to account for its complex magnetic nature [62].

the lattice expansion, the isobaric heat capacity and the slope of the bulk modulus as shown by the blue curves in Fig. 5. This demonstrates that anharmonic contributions to the vibrational free energy cannot be neglected for accurate thermodynamic property predictions in TaVCrW, especially at temperatures near the melting point, even though a qh-effective model is used as the reference. Including the effect of coupling to the total free energies partially compensates the strong anharmonic contribution, with the strength of the compensation depending on the specific thermodynamic quantity. It should be stressed that the change in thermodynamic properties represented by the shift from the blue to the black curves is not an effect of the free energy difference between MTP and DFT-low [which is very small as evidenced from Fig. 3(a)], but predominantly due to the temperature-dependent electronic free energy change coming from high-temperature vibrations (coupling effect). This shift in properties due to the coupling is also denoted by the black arrows shown only at 2500 K in Fig. 5.

In order to further emphasise the fact that vibrations have a strong impact on the high-temperature electronic free energy, especially in refractory systems, we explicitly indicate these values in Fig. 6. Here, the electronic free energy (Eq. 5) of the static lattice (shown in lighter shade) is compared to that obtained as an average from 5 different snapshots from an AIMD run at 2500 K. In these calculations, the electronic temperature corresponds to 2500 K. It is observed that, for the given point, the electronic free energy for TaVCrW changes by 13 meV/atom due to atomic vibrations. For comparison, results are also plotted for the corresponding refractory unaries at 2500 K. The change in the electronic free energy coming from vibrations can be related to the smearing of the electronic

density of states (DOS) at higher temperature and the value at the Fermi level as compared to the static electronic DOS. The qualitative change in the value of the DOS at the Fermi level at high temperature is different for Ta in comparison to V and W, and hence coupling reduces the electronic free energy in Ta. Based on such an analysis, one can also speculate how the static and smeared out electronic DOS would look for the TaVCrW system. The background behind the electronic free energies and coupling effects has been studied in thorough detail in Ref. [61]. The values in Fig. 6 indicate that the electron-phonon coupling term is likewise not negligible for accurate thermodynamic property predictions in these systems. As will be discussed later, these electronic free energy changes can be more efficiently captured by directly upsampling from the MTP. Once we have total DFT free energies at low accuracy, upsampling the energies to high parameter DFT accuracy has negligible effect on the thermodynamic properties as evidenced by magenta dots that fall on top of the black curves in Fig. 5.

#### D. Effect of the exchange-correlation functional

The thermodynamic properties were estimated using both GGA and LDA exchange-correlation functionals. Figure 7 illustrates the  $a_{\text{lat}}$ ,  $C_p$ , and  $B_T$  predicted using both functionals by the conventional TU-TILD method. Here, we show the calculated values up to MTP accuracy and including the coupling term up to full DFT accuracy. The exchange correlation has the same effect in both of these cases. As is the case with other metals and alloys [63–65], the LDA functional predicts a harder system with a higher  $B_T$  and smaller  $a_{\text{lat}}$  in comparison to GGA. The predicted  $C_p$  as the temperature nears the melting point becomes smaller for LDA than for GGA. Temperature has the same effect on the thermodynamic property predictions using either functionals.

#### E. Single MTP vs multiple MTPs

Here, we discuss the effect of using a single MTP in performing TU-TILD calculations across the entire temperature range as opposed to using multiple MTPs. In Sec. III A, we had shown the RMSE in energies and forces and  $\Delta F^{\text{MTP} \rightarrow \text{DFT}}$  (free energy difference between the MTP and DFT-low) to be the key quantities that affect the performance of the MTP in a TU-TILD methodology. Hence, we now compare these values at different temperatures while using four MTPs (based on the fitted temperature) and a single MTP across the full temperature range, see Fig. 8. For a particular temperature, the various dots represent increasing volume as one moves from left to right. Both the RMSEs and the free energy differences between MTP and DFT for all temperatures fall in the same range irrespective of the use of a single or multiple MTPs suggesting that they would be equally efficient in a TU-TILD scheme up to the melting point. The robustness of a single MTP fitted to high-temperature MD data facilitates an accurate prediction of thermodynamic properties, not only at temperatures near the fitted data, but across the entire temperature range. By using just a single MTP, we also reduce the number of initially expensive AIMD runs that are needed

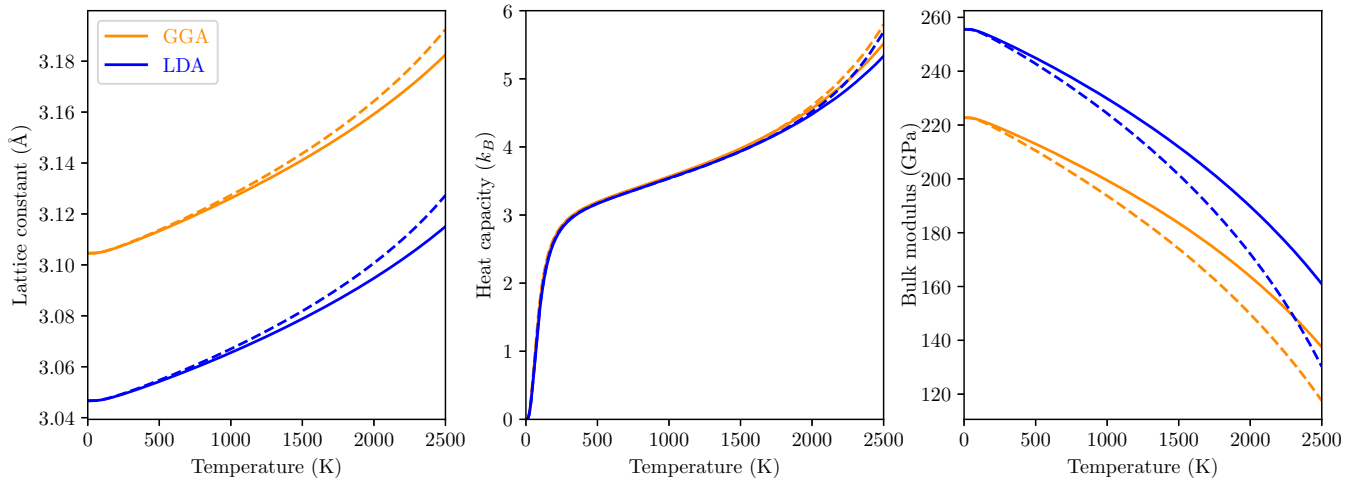


FIG. 7. Lattice constant, isobaric heat capacity and bulk modulus as a function of temperature for TaVCrW as predicted by TU-TILD using the GGA (orange) and the LDA (blue) exchange correlation functionals. Dashed curves correspond to the estimation up to the MTP level. The solid curves include additionally the adiabatic electron-phonon coupling implicit in the TI from MTP to DFT.

for fitting MTPs and the corresponding computational cost, without any loss of accuracy.

Using a single MTP has another additional benefit. The free energies calculated with a single MTP are smoother in  $V$  and  $T$  (this is already noticed in the change in  $\Delta F^{\text{MTP} \rightarrow \text{DFT}}$  values with volume at different temperatures in Fig. 8) and fitting an accurate surface to these values is accomplished more efficiently. The thermodynamic properties were also computed using the single MTP as the intermediate state. Crucially, as we shall see in the next section, there is no significant change in lattice constant, bulk modulus and isobaric heat capacity even while using a single MTP.

### F. Direct upsampling

The novelty compared to the conventional TU-TILD methodology that is proposed in this work is *direct upsampling* where upsampling was performed directly after the first stage of TU-TILD on configurations generated by the MTP. A comparison of the total vibrational free energy using the conventional TU-TILD using four MTPs across the temperature range and using direct upsampling using only the MTP-2500K across the entire temperature range with the GGA exchange-correlation functional for the entire grid of  $(V, T)$  points can be observed already in Fig. 1. The data points match within DFT accuracy even at high temperatures and large volumes.

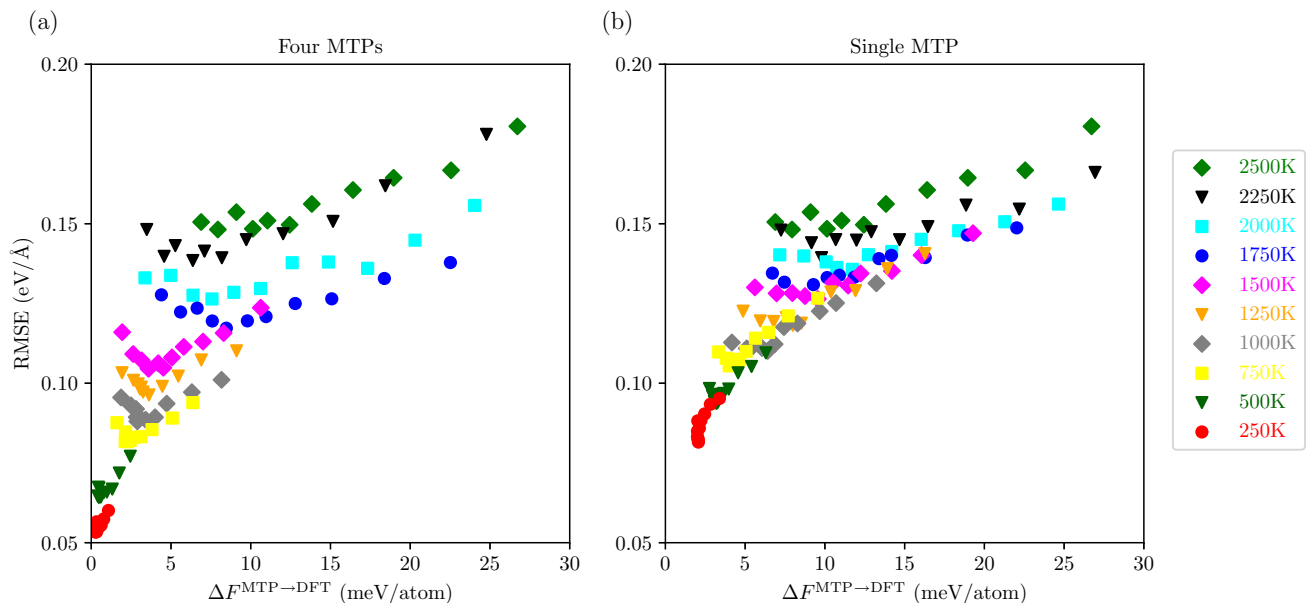


FIG. 8. Correlation of the RMSE in atomic forces and the free energy difference between MTP and DFT-low ( $\Delta F^{\text{MTP} \rightarrow \text{DFT}}$ ) calculated using (a) four MTPs and (b) a single MTP for all  $(V, T)$ . Symbols of the same color represent different volumes for a fixed temperature; generally, the volume increases from left to right.

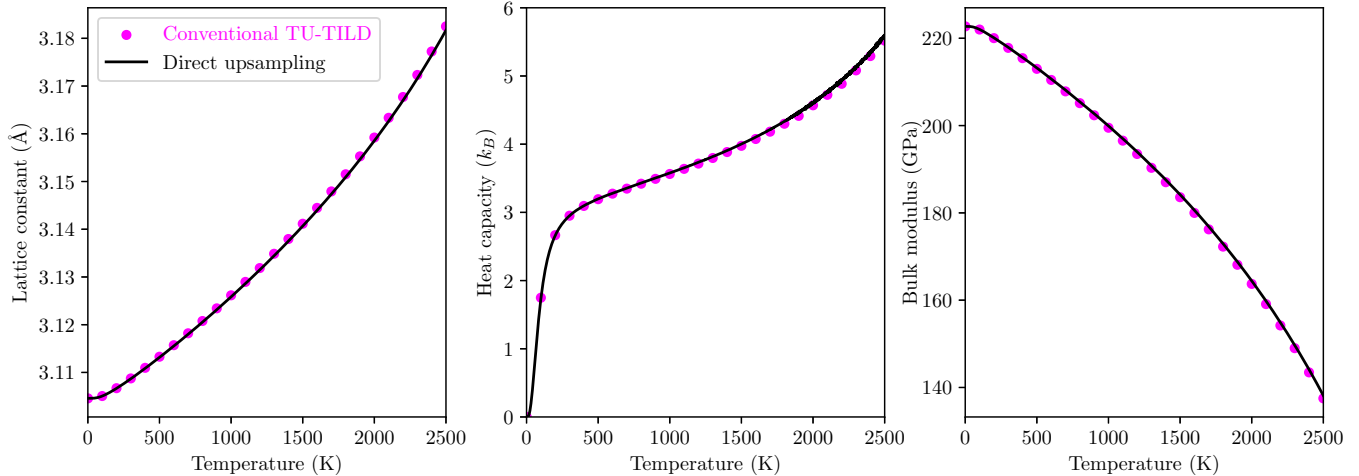


FIG. 9. Lattice constant, isobaric heat capacity and bulk modulus as a function of temperature for TaVCrW as predicted by direct upsampling using a single MTP fitted to 2500 K in comparison to the previously computed values using conventional TU-TILD.

This indicates that by performing direct upsampling using a single high-temperature fitted MTP, we achieved an accuracy of  $\pm 1.5$  meV/atom for full free energy points. A consequence of this is Fig. 9 which shows the thermodynamic properties predicted from direct upsampling using a single MTP, represented by the black lines. The results lie on top of the values predicted by the conventional TU-TILD method, represented by magenta dots. The dots are the same as the ones in Fig. 5.

Owing to the robustness of the MTPs, using only a single high-temperature fit MTP and performing direct upsampling tremendously reduces the computational cost of obtaining thermodynamic properties up to melting point to DFT accuracy. This is summarised in the next section.

### G. Computational costs

The computing resources consumed for the 128-atom quaternary system are listed in Table IV. Since we use a single MTP in comparison to four MTPs, the number of initial AIMD calculations reduces by one fourth. Besides this, the biggest gain in speed is achieved by avoiding the expensive

TABLE IV. Approximate computing time for thermodynamic properties up to melting point in a 128-atom TaVCrW SQS using conventional TU-TILD and direct upsampling. TI calculations are on a  $11 \times 10$  ( $V, T$ ) mesh. The time is in 1K core hours.

Contribution	Cost (TU-TILD with 4 MTPs)	New cost (Direct upsampling with 1 MTP)
$E_{0K}$	2	2
$F^{el}$	100	—
$F^{ref}$ (qh-effective)	—	12
AIMD for MTPs	100	25
$\Delta F^{ref \rightarrow MTP}$	15	15
$\Delta F^{MTP \rightarrow DFT}$	720	—
$\langle \Delta E \rangle^{up}$	210	—
$\langle \Delta E \rangle^{up-new}$	—	210
Total	$\approx 1100$	$\approx 260$

second stage of the TU-TILD formalism (TI from the interatomic potential to low parameter DFT). Static electronic free energy calculations are also avoided since the temperature-dependent electronic free energy is included during direct upsampling.

## IV. CONCLUSIONS

Thermodynamic properties of the low activation TaVCrW MPCA have been computed *ab initio* up to 2500 K. Assuming a fully disordered BCC system, we have included all relevant finite temperature excitations: electronic, harmonic, anharmonic and (adiabatic) electron-phonon coupling. The static electronic free energy at high temperatures is considerable in this alloy, similar to what is observed for its refractory unary endmembers, and it significantly affects thermodynamic properties (particularly the heat capacity). The effective harmonic model obtained from a fit to *ab initio* molecular dynamic forces at 500 K does not account for all vibrational interactions. As temperature increases, a substantial anharmonic contribution to the vibrational free energy and the resulting thermodynamic properties is observed. The effect of anharmonicity is found to be as critical as the static electronic contribution. In addition, high-temperature vibrations couple to the electronic free energy in this alloy, again in line with the refractory unaries that it contains. Thus, to reach DFT accuracy in the final property predictions, this effect is non-negligible and has to be taken into account.

To achieve the just summarized results for a disordered, chemically complex MPCA efficiently, we have exploited the predictive capabilities of moment tensor potentials (MTPs) in a conventional *two-stage upsampled thermodynamic integration using Langevin dynamics* (TU-TILD) methodology. The MTPs have been fitted to high-temperature *ab initio* data to this end. An extensive analysis of the various stages of TU-TILD in calculating free energies up to the melting point has been performed. The choice of the initial reference to approximate the vibrational free energy of the solid does not affect the final free energy. However, from a practical perspective, an effective harmonic reference provides an ideal interplay

between fitting time and the eventual time needed for statistical convergence of free energy calculations during thermodynamic integration and serves as the optimum reference. Owing to the robustness and superior performance of MTPs, we have also proposed a computationally cheaper modification to the TU-TILD methodology referred to as *direct upsampling*. Here, the free energy difference to high-parameter DFT across the entire temperature range is calculated directly on configurations generated by a single high-temperature fitted MTP, thereby avoiding the highly expensive second-stage of TU-TILD and reducing the total computational cost by 75%.

In addition to the properties predicted for the TaVCrW alloy, the benefits of the current study are twofold. First, the performance of the MTP in predicting the configurational phase space even for a complex system such as a disordered HEA asserts its application for other systems. Secondly, through the in-depth analysis and comparison to the conventional methodology conducted herein, our modified formalism is well positioned for thermodynamic property prediction and high-throughput screening of other MPCAs. The methodology will be extended to investigate other low activation HEAs and nonstoichiometric systems in forthcoming articles.

## ACKNOWLEDGMENTS

This work was supported by United Kingdom EPSRC Grant No. EP/S032819/1 and EP/S032835/1, Loughborough's High Performance Computing unit and ARCHER UK National Supercomputing Service. Via our membership of the UK's HEC Materials Chemistry Consortium, which is funded by EPSRC (EP/L000202), this work used the UK Materials and Molecular Modelling Hub for computational resources, MMM Hub, which is partially funded by EPSRC (EP/P020194 and EP/T022213). P.S. would like to thank the Alexander von Humboldt Foundation for their support through the Alexander von Humboldt Postdoctoral Fellowship Program. F.K. acknowledges support by the Nederlandse Organisatie voor Wetenschappelijk Onderzoek (NWO) (VIDI Grant No. 15707). B.G. acknowledges funding from the European Research Council (ERC) under the European Unions Horizon 2020 research and innovation programme (Grant Agreement No. No 865855) and support by the Stuttgart Centre for Simulation Science (SimTech). F.K. and B.G. acknowledge support from the collaborative DFG-RFBR Grant (Grants No. DFG KO 5080/3-1, No. DFG GR 3716/6-1).

- 
- [1] J.-W. Yeh, S.-K. Chen, S.-J. Lin, J.-Y. Gan, T.-S. Chin, T.-T. Shun, C.-H. Tsau, and S.-Y. Chang, Nanostructured high-entropy alloys with multiple principal elements: novel alloy design concepts and outcomes, *Advanced Engineering Materials* **6**, 299 (2004).
- [2] M.-H. Tsai and J.-W. Yeh, High-entropy alloys: a critical review, *Mater. Res. Lett.* **2**, 107 (2014).
- [3] K. Murty and I. Charit, Structural materials for Gen-IV nuclear reactors: Challenges and opportunities, *J. Nucl. Mater.* **383**, 189 (2008).
- [4] S. J. Zinkle and G. Was, Materials challenges in nuclear energy, *Acta Mater.* **61**, 735 (2013).
- [5] S. J. Zinkle and J. T. Busby, Structural materials for fission & fusion energy, *Mater. Today* **12**, 12 (2009).
- [6] A. Kareer, J. Waite, B. Li, A. Couet, D. Armstrong, and A. Wilkinson, Low activation, refractory, high entropy alloys for nuclear applications, *J. Nucl. Mater.* **526**, 151744 (2019).
- [7] A. Ayyagari, R. Salloom, S. Muskeri, and S. Mukherjee, Low activation high entropy alloys for next generation nuclear applications, *Materialia* **4**, 99 (2018).
- [8] A. Kohyama, A. Hishinuma, D. Gelles, R. Klueh, W. Dietz, and K. Ehrlich, Low-activation ferritic and martensitic steels for fusion application, *J. Nucl. Mater.* **233-237**, 138 (1996).
- [9] M. R. Gilbert, M. Fleming, and J.-C. Sublet, Automated inventory and material science scoping calculations under fission and fusion conditions, *Nuclear Engineering and Technology* **49**, 1346 (2017).
- [10] P. Barron, A. Carruthers, J. Fellowes, N. Jones, H. Dawson, and E. Pickering, Towards V-based high-entropy alloys for nuclear fusion applications, *Scr. Mater.* **176**, 12 (2020).
- [11] O. El-Atwani, N. Li, M. Li, A. Devaraj, J. K. S. Baldwin, M. M. Schneider, D. Sobieraj, J. S. Wróbel, D. Nguyen-Manh, S. A. Maloy, and E. Martinez, Outstanding radiation resistance of tungsten-based high-entropy alloys, *Sci. Adv.* **5**, eaav2002 (2019).
- [12] D. Sobieraj, J. S. Wróbel, T. Rygier, K. J. Kurzydłowski, O. El Atwani, A. Devaraj, E. M. Saez, and D. Nguyen-Manh, Chemical short-range order in derivative Cr-Ta-Ti-V-W high entropy alloys from the first-principles thermodynamic study, *Phys. Chem. Chem. Phys.* **22**, 23929 (2020).
- [13] B. Grabowski, L. Ismer, T. Hickel, and J. Neugebauer, *Ab initio* up to the melting point: Anharmonicity and vacancies in aluminum, *Phys. Rev. B* **79**, 134106 (2009).
- [14] S. Baroni, P. Giannozzi, and E. Isaev, Density-functional perturbation theory for quasi-harmonic calculations, *Reviews in Mineralogy and Geochemistry* **71**, 39 (2010).
- [15] A. Togo and I. Tanaka, First principles phonon calculations in materials science, *Scr. Mater.* **108**, 1 (2015).
- [16] A. Glensk, B. Grabowski, T. Hickel, and J. Neugebauer, Breakdown of the Arrhenius Law in Describing Vacancy Formation Energies: The Importance of Local Anharmonicity Revealed by *Ab initio* Thermodynamics, *Phys. Rev. X* **4**, 011018 (2014).
- [17] P. Souvatzis, O. Eriksson, M. Katsnelson, and S. Rudin, Entropy Driven Stabilization of Energetically Unstable Crystal Structures Explained from First Principles Theory, *Phys. Rev. Lett.* **100**, 095901 (2008).
- [18] P. Souvatzis, O. Eriksson, M. Katsnelson, and S. Rudin, The self-consistent *ab initio* lattice dynamical method, *Comput. Mater. Sci.* **44**, 888 (2009).
- [19] O. Hellman, P. Steneteg, I. A. Abrikosov, and S. I. Simak, Temperature dependent effective potential method for accurate free energy calculations of solids, *Phys. Rev. B* **87**, 104111 (2013).
- [20] I. Errea, M. Calandra, and F. Mauri, Anharmonic free energies and phonon dispersions from the stochastic self-consistent harmonic approximation: Application to platinum and palladium hydrides, *Phys. Rev. B* **89**, 064302 (2014).

- [21] T. Sun, D.-B. Zhang, and R. M. Wentzcovitch, Dynamic stabilization of cubic CaSiO<sub>3</sub> perovskite at high temperatures and pressures from *ab initio* molecular dynamics, *Phys. Rev. B* **89**, 094109 (2014).
- [22] A. Carreras, A. Togo, and I. Tanaka, Dynaphopy: A code for extracting phonon quasiparticles from molecular dynamics simulations, *Comput. Phys. Commun.* **221**, 221 (2017).
- [23] A. I. Duff, T. Davey, D. Korbmayer, A. Glensk, B. Grabowski, J. Neugebauer, and M. W. Finnis, Improved method of calculating *ab initio* high-temperature thermodynamic properties with application to ZrC, *Phys. Rev. B* **91**, 214311 (2015).
- [24] T. A. Mellan, A. I. Duff, B. Grabowski, and M. W. Finnis, Fast anharmonic free energy method with an application to vacancies in ZrC, *Phys. Rev. B* **100**, 024303 (2019).
- [25] A. I. Duff, M. Finnis, P. Maugis, B. J. Thijsse, and M. H. Sluiter, MEAMfit: A reference-free modified embedded atom method (RF-MEAM) energy and force-fitting code, *Comput. Phys. Commun.* **196**, 439 (2015).
- [26] X. Zhang, B. Grabowski, T. Hickel, and J. Neugebauer, Calculating free energies of point defects from *ab initio*, *Comput. Mater. Sci.* **148**, 249 (2018).
- [27] A. Forslund and A. Ruban, *Ab initio* surface free energies of tungsten with full account of thermal excitations, *Phys. Rev. B* **105**, 045403 (2022).
- [28] B. Grabowski, Y. Ikeda, P. Srinivasan, F. Körmann, C. Freysoldt, A. I. Duff, A. Shapeev, and J. Neugebauer, *Ab initio* vibrational free energies including anharmonicity for multicomponent alloys, *npj Comput. Mater.* **5**, 80 (2019).
- [29] M. S. Daw and M. I. Baskes, Embedded-atom method: Derivation and application to impurities, surfaces, and other defects in metals, *Phys. Rev. B* **29**, 6443 (1984).
- [30] M. Finnis and J. Sinclair, A simple empirical N-body potential for transition metals, *Philosophical Magazine A* **50**, 45 (1984).
- [31] A. Zunger, S.-H. Wei, L. G. Ferreira, and J. E. Bernard, Special Quasirandom Structures, *Phys. Rev. Lett.* **65**, 353 (1990).
- [32] P. A. Varotsos, K. D. Alexopoulos, and R. O. Simmons, Thermodynamics of point defects and their relation with bulk properties, *Phys. Today* **40**(11), 95 (1987).
- [33] B. Grabowski, P. Söderlind, T. Hickel, and J. Neugebauer, Temperature-driven phase transitions from first principles including all relevant excitations: The fcc-to-bcc transition in Ca, *Phys. Rev. B* **84**, 214107 (2011).
- [34] G. Kresse and J. Hafner, *Ab initio* molecular dynamics for liquid metals, *Phys. Rev. B* **47**, 558 (1993).
- [35] G. Kresse and J. Hafner, *Ab initio* molecular-dynamics simulation of the liquid-metal–amorphous-semiconductor transition in germanium, *Phys. Rev. B* **49**, 14251 (1994).
- [36] G. Kresse and J. Furthmüller, Efficient iterative schemes for *ab initio* total-energy calculations using a plane-wave basis set, *Phys. Rev. B* **54**, 11169 (1996).
- [37] G. Kresse and J. Furthmüller, Efficiency of *ab-initio* total energy calculations for metals and semiconductors using a plane-wave basis set, *Comput. Mater. Sci.* **6**, 15 (1996).
- [38] P. E. Blöchl, Projector augmented-wave method, *Phys. Rev. B* **50**, 17953 (1994).
- [39] G. Kresse and D. Joubert, From ultrasoft pseudopotentials to the projector augmented-wave method, *Phys. Rev. B* **59**, 1758 (1999).
- [40] P. Vinet, J. R. Smith, J. Ferrante, and J. H. Rose, Temperature effects on the universal equation of state of solids, *Phys. Rev. B* **35**, 1945 (1987).
- [41] N. D. Mermin, Thermal properties of the inhomogeneous electron gas, *Phys. Rev.* **137**, A1441 (1965).
- [42] K. Parlinski, Z. Li, and Y. Kawazoe, First-Principles Determination of the Soft Mode in Cubic ZrO<sub>2</sub>, *Phys. Rev. Lett.* **78**, 4063 (1997).
- [43] D. Alfè, G. Price, and M. Gillan, Thermodynamics of hexagonal-close-packed iron under earths core conditions, *Phys. Rev. B* **64**, 045123 (2001).
- [44] A. Einstein, Die plancksche theorie der strahlung und die theorie der spezifischen wärme, *Annalen der Physik* **327**, 180 (1907).
- [45] O. Hellman and I. A. Abrikosov, Temperature-dependent effective third-order interatomic force constants from first principles, *Phys. Rev. B* **88**, 144301 (2013).
- [46] S. Boeck, C. Freysoldt, A. Dick, L. Ismer, and J. Neugebauer, The object-oriented DFT program library S/PHI/nX, *Comput. Phys. Commun.* **182**, 543 (2011).
- [47] R. Wallace and R. G. Wallace, Information theory, scaling laws and the thermodynamics of evolution, *J. Theor. Biol.* **192**, 545 (1998).
- [48] M. T. Dove, *Introduction to Lattice Dynamics*, Cambridge Topics in Mineral Physics and Chemistry (Cambridge University Press, Cambridge, 1993), Vol. 4.
- [49] J.-P. Riviere, Radiation induced point defects and diffusion, in *Application of Particle and Laser Beams in Materials Technology* (Springer, Dordrecht, 1995), pp. 53–76.
- [50] L.-F. Zhu, B. Grabowski, and J. Neugebauer, Efficient approach to compute melting properties fully from *ab initio* with application to cu, *Phys. Rev. B* **96**, 224202 (2017).
- [51] S. Plimpton, Fast parallel algorithms for short-range molecular dynamics, *J. Comput. Phys.* **117**, 1 (1995).
- [52] S. Plimpton, P. Crozier, and A. Thompson, LAMMPS-large-scale atomic/molecular massively parallel simulator, *Sandia National Laboratories* **18**, 43 (2007).
- [53] A. V. Shapeev, Moment tensor potentials: A class of systematically improvable interatomic potentials, *Multiscale Modeling & Simulation* **14**, 1153 (2016).
- [54] C. Nyshadham, M. Rupp, B. Bekker, A. V. Shapeev, T. Mueller, C. W. Rosenbrock, G. Csányi, D. W. Wingate, and G. L. Hart, Machine-learned multi-system surrogate models for materials prediction, *npj Comput. Mater.* **5**, 51 (2019).
- [55] I. S. Novikov, K. Gubaev, E. V. Podryabinkin, and A. V. Shapeev, The MLIP package: moment tensor potentials with MPI and active learning, *Machine Learning: Science and Technology* **2**, 025002 (2020).
- [56] V. Moruzzi, J. Janak, and K. Schwarz, Calculated thermal properties of metals, *Phys. Rev. B* **37**, 790 (1988).
- [57] L. Vegard, Die konstitution der mischkristalle und die raumfüllung der atome, *Z. Phys.* **5**, 17 (1921).
- [58] D. Bolef and J. De Klerk, Anomalies in the elastic constants and thermal expansion of chromium single crystals, *Phys. Rev.* **129**, 1063 (1963).
- [59] F. H. Featherston and J. Neighbours, Elastic constants of tantalum, tungsten, and molybdenum, *Phys. Rev.* **130**, 1324 (1963).
- [60] J. Greiner, O. Carlson, and J. Smith, Single-crystal elastic constants of vanadium and vanadium with oxygen additions, *J. Appl. Phys.* **50**, 4394 (1979).

- [61] X. Zhang, B. Grabowski, F. Körmann, C. Freysoldt, and J. Neugebauer, Accurate electronic free energies of the 3 d, 4 d, and 5 d transition metals at high temperatures, *Phys. Rev. B* **95**, 165126 (2017).
- [62] F Körmann, B. Grabowski, P. Sderlind, M. Palumbo, S. G. Fries, T. Hickel, and J. Neugebauer, Thermodynamic modeling of chromium: strong and weak magnetic coupling, *J. Phys.: Condens. Matter* **25**, 425401 (2013).
- [63] Z. Lin, L. V. Zhigilei, and V. Celli, Electron-phonon coupling and electron heat capacity of metals under conditions of strong electron-phonon nonequilibrium, *Phys. Rev. B* **77**, 075133 (2008).
- [64] B. Grabowski, T. Hickel, and J. Neugebauer, *Ab initio* study of the thermodynamic properties of nonmagnetic elementary fcc metals: Exchange-correlation-related error bars and chemical trends, *Phys. Rev. B* **76**, 024309 (2007).
- [65] D. Ma, B. Grabowski, F. Körmann, J. Neugebauer, and D. Raabe, *Ab initio* thermodynamics of the CoCrFeMnNi high entropy alloy: Importance of entropy contributions beyond the configurational one, *Acta Mater.* **100**, 90 (2015).